

# ZnSb Polymorphs with Improved Thermoelectric Properties

Maximilian Amsler,<sup>†</sup> Stefan Goedecker,<sup>\*,‡</sup> Wolfgang G. Zeier,<sup>¶</sup> G. Jeffrey Snyder,<sup>†</sup> Chris Wolverton,<sup>†</sup> and Laurent Chaput<sup>\*,§</sup>

<sup>†</sup>Department of Materials Science and Engineering, Northwestern University, Evanston, Illinois 60208, United States

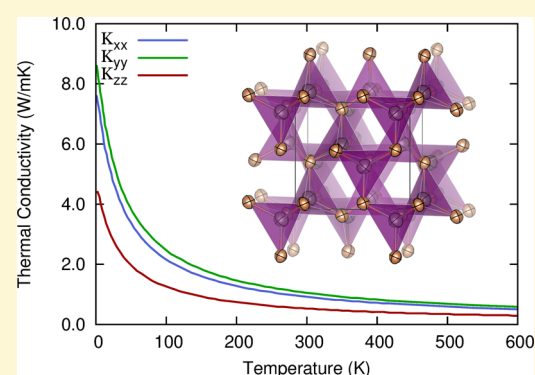
<sup>‡</sup>Department of Physics, Universität Basel, Klingelbergstr. 82, 4056 Basel, Switzerland

<sup>¶</sup>Physikalisch-Chemisches Institut, Justus-Liebig-Universität Giessen, Heinrich-Buff-Ring 58, 35392 Giessen, Germany

<sup>§</sup>Université de Lorraine, LEMTA, Centre National de la Recherche Scientifique, Unité Mixte de Recherche 7563, BP 70239, 54506 Vandœuvre Cedex, France

## Supporting Information

**ABSTRACT:**  $\text{Zn}_x\text{Sb}_{1-x}$  systems are one of the most promising materials for thermoelectric applications due to their low cost, low toxicity, and high thermoelectric figure of merit. We report the discovery and characterization of novel ZnSb polymorphs with improved thermoelectric properties from a systematic *ab initio* structural search. The putative ground state at low temperature is a structure with *Pbca* symmetry. Corresponding electron and phonon transport properties are computed, where the lattice thermal conductivity was accurately obtained through third-order interatomic force constants. At 500 K, both the reduced figure of merit  $S^2/L$  as well as the lattice thermal conductivity are superior to any previously reported numbers on ZnSb polymorphs, rendering the *Pbca* phase a promising candidate for an exceptionally good thermoelectric material.



## INTRODUCTION

Global energy challenges and limited fossil fuel demands the exploration of new sustainable energy resources, which has recently led to intense research in thermoelectric (TE) materials. The transformation of thermal to electric energy could unlock the potential to harvest clean power from natural or waste heat.<sup>1</sup> The efficiency of heat conversion is governed<sup>2</sup> by the dimensionless figure of merit  $ZT = \sigma S^2 T / \kappa$ , where  $T$  is the absolute temperature (K),  $S$  is the thermopower (V/K),  $\sigma$  is the electrical conductivity (S/m), and  $\kappa$  is the thermal conductivity (W/Km). Thus, maximizing  $ZT$  requires the simultaneous optimization of conflicting material properties (maximizing  $S$  and  $\sigma$  while minimizing  $\kappa$ ), posing a nontrivial materials design challenge. A plethora of strategies have been demonstrated to enhance TE efficiency, e.g., by increasing the carrier density through heavy doping of semiconductors and reducing the lattice thermal conductivity through intrinsic anharmonicity (such as  $\text{SnSe}$ ), structural disorder (such as alloying  $\text{Bi}_2\text{Te}_3$ ) and complexity (such as  $\text{Zn}_4\text{Sb}_3$ ), nanostructuring (such as  $\text{PbTe}$ ), or substructuring (skutterudites and clathrates<sup>7–9</sup>).

Alloys and compounds based on Zn and Sb have been studied already by Seebeck as early as the beginning of the 19th century<sup>10</sup> and are touted as promising high- $ZT$  materials due to their abundance, nontoxicity, and low cost. Materials with stoichiometries of ZnSb and  $\text{Zn}_4\text{Sb}_3$  have been well studied,<sup>1,5,11–13</sup> the latter revealing a remarkably high  $ZT$  of  $\approx 1.4$  at 670 K which can be mainly attributed to the low lattice

thermal conductivity due to the high complexity in the atomic structure.<sup>14,15</sup> Other materials with different stoichiometries such as  $\text{Zn}_8\text{Sb}_7$  and metastable phases have also recently been reported in the literature.<sup>14,16–18</sup> Although the ZnSb alloy at its equiatomic composition has not drawn as much attention as other phases, it shows promising TE properties with a  $ZT$  of 0.8 at 573 K in hot-pressed samples.<sup>19</sup> The value of  $ZT$  was shown to increase upon doping with Cu and through nanostructuring with  $\text{Zn}_3\text{P}_2$  toward a value of 1 at 550 K<sup>20</sup> and to  $ZT = 1.15$  at 670 K by Ag doping and  $\text{Ag}_3\text{Sb}$  nanostructuring.<sup>21</sup> Recently, the thermal and vibrational properties were extensively studied from Raman spectroscopy<sup>22</sup> and single crystal and powder X-ray diffraction (XRD).<sup>22,23</sup> Above all, the most compelling advantage of ZnSb over other stoichiometries and phases lies in its stability.<sup>24</sup> In contrast,  $\beta\text{-Zn}_4\text{Sb}_3$  for example undergoes phase transitions upon both cooling and heating and is prone to either elemental decomposition or into ZnSb + Sb during thermal cycling, whereas ZnSb is stable in a wide temperature and pressure range.

ZnSb is known to crystallize in an orthorhombic *Pbca* phase<sup>25</sup> with the same structure as CdSb, and recent low temperature single crystal X-ray diffraction (XRD) experiments confirm its crystal structure.<sup>22</sup> Although no phase transition has been observed below the melting temperature in contrast to

Received: October 2, 2015

Revised: March 7, 2016

Published: March 7, 2016

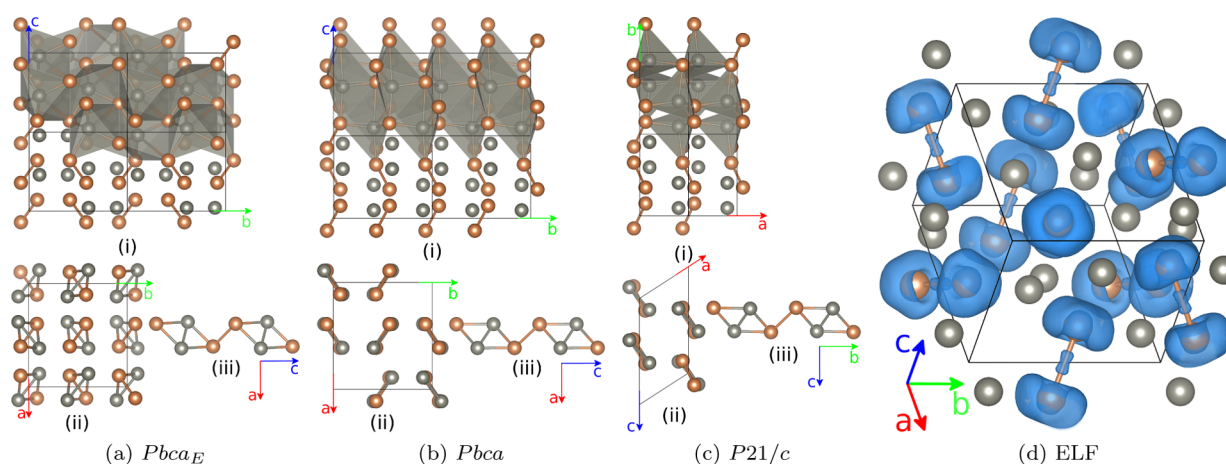


**Figure 1.** Structures of the various ZnSb phases. Panel (a) shows the experimental phase along the  $x$  and  $z$  axis ((i) and (ii), respectively), while panel (b) shows the putative ground state structure along the  $x$  and  $z$  axis ((i) and (ii), respectively). Panel (c) shows the  $P21/c$  phase along the  $z$  and  $y$  axis in (i) and (ii). The subpanels (iii) show the chains of diamond moieties from the side (whereas in (ii) the view is along the chains). The ELF at a value of 0.76 is shown in panel (d) for the  $Pbca$  phase viewed along the central  $Sb_2^{4-}$  dimer. Zn and Sb atoms are denoted with gray and copper spheres, respectively.

other compositions in  $Zn_xSb_{1-x}$  alloys<sup>24</sup> at ambient pressure, ZnSb undergoes a phase transition to a simple hexagonal structure, as well as decomposition and amorphization upon applying and unloading high pressure.<sup>26,27</sup> Furthermore, the XRD pattern from thin-film samples shows evidence for the formation of a yet unknown metastable crystalline phase of zinc antimonide.<sup>14</sup> These findings clearly indicate a complex energy landscape and possible polymorphism in ZnSb, motivating further investigation of the low energy phase diagram of ZnSb.

## RESULTS AND DISCUSSION

To map out the low energy phase diagram of the ZnSb system, the enthalpy landscape was systematically explored by a sophisticated structural prediction method (minima hopping method<sup>28,29</sup>) based on first-principles density functional theory (DFT) calculations with the Perdew–Burke–Ernzerhof (PBE) generalized gradient (GGA) exchange–correlation (XC) functional. The structural searches were performed at both ambient condition and high pressures up to 20 GPa. During the search, the experimental orthorhombic structure was retrieved at a volume of 25.28 Å<sup>3</sup> per atom (see Figure 1a and Table 1). GGA functionals are well-known to overestimate the lattice constants, such that the computed volume is slightly larger than the experimentally observed value of 23.98 Å<sup>3</sup> per atom.<sup>22</sup>

**Table 1.** Structural Data for the  $Pbca$  and  $Pbca_E$  Phases, with Lattice Parameters  $a$ ,  $b$ , and  $c$  Together with the Experimental Lattice Parameters Retrieved from Fischer et al.<sup>22</sup> at 9 K<sup>a</sup>

$Pbca$	$a = 8.397$ Å	$b = 7.767$ Å	$c = 6.506$ Å
Zn	0.1117	0.4076	0.4035
Sb	0.3904	0.5678	0.3484
$Pbca_E$	$a = 8.232$ Å	$b = 7.812$ Å	$c = 6.286$ Å
EXP	$a = 8.079$ Å	$b = 7.709$ Å	$c = 6.161$ Å
Zn	0.1275	0.3937	0.4590
Sb	0.3912	0.5829	0.3583

<sup>a</sup>The fractional coordinates are at the general Wyckoff positions 8c for the Zn and Sb atoms.

Furthermore, many different structures were discovered with extremely low enthalpies at ambient pressure. A novel, hitherto unreported structure was found with the same space group as the experimental structure with a formation energy lower by 4 meV/f.u. compared to the experimental phase. Thus, from hereon, the experimental phase will be referred to as  $Pbca_E$ , while the novel putative ground state will be simply referred to as  $Pbca$  (see Figure 1b). Although the exact energetic ordering between  $Pbca_E$  and  $Pbca$  depends on the XC functional employed in the DFT calculations, the energy difference consistently lies within less than 14 meV/f.u., confirming that the two phases are at least degenerate in energy (see the Supporting Information). Another phase with higher thermodynamic stability than  $Pbca_E$  was found with  $P21/c$  symmetry (see Figure 1c) with a formation energy of 0.5 meV/f.u. below  $Pbca_E$ . Furthermore, several other polytypes were discovered within a small energy range of a few tens of meV/f.u. above  $Pbca_E$ , indicating a large structural diversity in a tight energy range. Such high configurational density is typical for glass-like energy landscapes<sup>30</sup> and supports the electron-crystal-phonon-glass concept in ZnSb compounds.<sup>5</sup> A rather peculiar cubic phase was found at about 65 meV/f.u. above  $Pbca_E$ . The crystal symmetry corresponds to the space group  $Pa\bar{3}$  and is related to  $Pbca_E$  through small structural distortions, and it transforms into this phase upon compression at around 10 GPa, indicating a second-order phase transition. A structure with  $Cmcm$  symmetry was found which becomes more stable than the experimental phase at about 6 GPa. However, according to our calculations, the decomposition into elemental Zn and Sb is favored above approximately 3 GPa, as illustrated in Figure 2 where the enthalpies of several phases are plotted as a function of pressure with respect to  $Pbca_E$ . Experimentally, ZnSb first amorphizes upon compression, decomposes, and then recrystallizes at about 7 GPa in a simple hexagonal (SH) phase of a different composition and a small quantity of elemental Zn.<sup>26,27</sup> Although we did not include the SH phase in our enthalpy phase diagram, the decomposition behavior is well captured by the enthalpy plot. To ensure dynamical stability, phonon calculations were carried out to make sure that no imaginary phonons were observed in the Brillouin zones in any of the above phases.

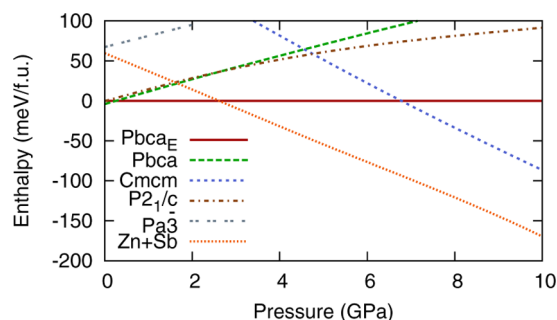


**Figure 2.** Enthalpies as a function of pressure of various competing ZnSb phases with respect to  $Pbca_E$ . The elemental energy for Zn was taken from the experimental hcp-structure.<sup>32</sup> The phase diagram of elemental Sb is more complicated, where phase transitions occur from  $R3m$ <sup>33</sup> to  $Pm3m$ <sup>34</sup> and finally to  $Im3m$ <sup>35</sup> upon applying pressure.

The lattice parameters and atomic coordinates of  $Pbca$  are given in Table 1, resulting in a volume of  $26.52 \text{ \AA}^3$  per atom. Qualitatively, the structure in ZnSb can be explained by the Zintl concept, where  $Zn^{2+}$  act as electron donors and  $Sb^{2-}$  accept electrons in addition to forming  $Sb_2^{4-}$  dimers to satisfy the octet rule. Therefore, it would be formally more appropriate to consider this phase as  $Zn_2Sb_2$  with  $Sb_2^{4-}$  building blocks intercalated with  $Zn^{2+}$  cations. The electron localization function (ELF) of  $Pbca$  in Figure 1d supports this picture where the lone electron pairs in the vicinity of the Sb atoms can be clearly seen as well as the localization of charge between them which contribute to the formation of covalent  $Sb_2^{4-}$  dimers. However, the validity of the Zintl concept in ZnSb compounds has been the subject of controversy due to the rather negligible amount of charge transfer of  $0.27 q_e$  per ion based on Bader charge analysis in  $Pbca_E$ .<sup>31</sup> The structural differences between  $Pbca$  and  $Pbca_E$  consist primarily of a rearrangement of  $Sb_2^{4-}$  and  $Zn^{2+}$  units, leading to distinct differences in the XRD patterns despite having the same space group (see Figure 3). In both the  $Pbca_E$  and  $Pbca$  phases, the

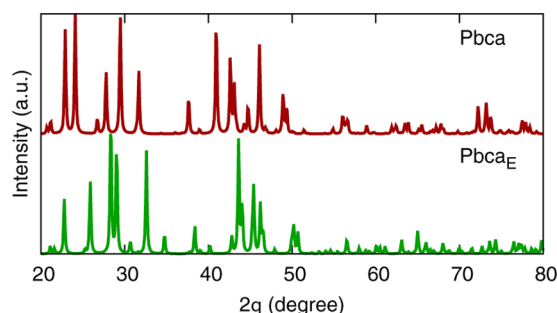


**Figure 3.** Simulated XRD pattern for the  $Pbca$  (red) and  $Pbca_E$  (green) phases with the radiation source of Cu K $\alpha$  with a wavelength of  $1.54056 \text{ \AA}$ .

$Sb_2^{4-}$  distances are almost identical ( $2.89 \text{ \AA}$  in  $Pbca$  and  $2.84 \text{ \AA}$  in  $Pbca_E$ ), and each atom is surrounded by 1 of the same and 4 of the opposite type, which leads to planar rhomboidal  $Zn_2Sb_2$ -rings and tetrahedra sharing edges and corners<sup>11</sup> (Figure S1a). Figure S1b,c shows the 5-fold coordination of Sb atoms together with the planar rings. In  $Pbca_E$ , the  $Zn_2Sb_2$  ring is almost orthogonal to the remaining zinc bond, while in  $Pbca$  it is rotated and nearly coplanar with the zinc bond. This rearrangement can also be seen from the panels (ii) and (iii) in Figure 1, showing the orientation of the rhomboidal chains

which are either coplanar ( $Pbca$  and  $P2_1/c$ ) or twisted ( $Pbca_E$ ): the subpanels (ii) and (iii) show the views along and from the side of the chains, respectively.

Another evidence for the formation of  $Sb_2^{4-}$  and Zn–Zn dimers in the rhomboidal chains of the various phases can be found when analyzing the phonon eigenmodes at the  $\Gamma$  point. The lowest energy eigenmodes consistently correspond to collective motions of the dimers, which either lead to translational, twisting, or expanding/contracting motions of the rhomboidal chains. In contrast to the study by Schweika et al.<sup>36</sup> on  $Zn_4Sb_3$  who ascribed low energy phonons to rattling of the  $Sb_2^{4-}$  dumbbells, our results show that Zn-vibrations contribute equally to low eigenmodes, which is in agreement with the results of Jund et al.<sup>37</sup> and Bjerg et al.<sup>13</sup> For  $Pbca_E$ , the lowest optical eigenmodes consist of both Sb and Zn dimer translations, where each pair of atoms associated with a dimer oscillates in the same direction around the equilibrium position. The first rotational modes of dimers are observed at phonons above  $1.43 \text{ THz}$ . Similarly, the  $Pbca$  exhibits dimer motions; however, the two lowest modes correspond to collective translations of the whole rhomboidal chain. The first libration mode is observed at frequencies as low as  $1.27 \text{ THz}$ . For the  $P2_1/c$  phase, the onset of dimer rotation occurs at even lower frequencies of around  $1.14 \text{ THz}$ . On the other hand, dimer-stretching modes, especially of the  $Sb_2^{4-}$  dimers, are only observed at higher energies above  $4.00 \text{ THz}$  for all phases.

With the phonon calculations at hand, the free energy was computed within the harmonic approximation to assess the stability of the different polymorphs at finite temperature and ambient pressure. From the free energy plot shown in Figure 5, we can deduce why the  $Pbca_E$  phase is observed experimentally: although the novel structure  $Pbca$  is favored at low temperatures, at higher temperatures,  $Pbca_E$  is stabilized by entropic effects. The transition temperature is located within the operating temperature range for heat conversion in TE materials. Similarly, the  $P2_1/c$  phase is slightly less stable than  $Pbca_E$  due to the phonon contribution. However, these results must be treated with caution, since anharmonic effects will become increasingly important at high temperatures.

Fischer et al. recently conducted an extensive survey of the thermal and vibrational properties in ZnSb through multi-temperature XRD measurements and DFT calculations in a wide temperature range.<sup>22</sup> The thermal dependence of the structural properties was extracted from single crystal XRD (SCXRD) measurements between  $9$  and  $400 \text{ K}$  and powder XRD (PXRD) measurements between  $300$  and  $723 \text{ K}$ . Similarly, Blichfeld and Iversen<sup>23</sup> performed multitemperature PXRD experiments between  $100$  and  $1000 \text{ K}$ . To compare the thermal lattice expansion, we calculated the cell volume as a function of temperature within the quasi-harmonic approximation, resulting in a theoretical thermal expansion coefficient at  $300 \text{ K}$  of  $\alpha_V^{Pbca_E} = 4.49 \times 10^{-5} \text{ K}^{-1}$  for the  $Pbca_E$  phase. This value is in good agreement with the experimental results of  $\alpha_V^{EXP} = 4.15 \times 10^{-5} \text{ K}^{-1}$  and  $\alpha_V^{EXP} = 3.59 \times 10^{-5} \text{ K}^{-1}$  from Fischer et al.<sup>22</sup> and Blichfeld and Iversen,<sup>23</sup> respectively. The new  $Pbca$  phase exhibits an expansion coefficient of  $\alpha_V^{Pbca} = 4.55 \times 10^{-5} \text{ K}^{-1}$ , which is very close to  $\alpha_V^{Pbca_E}$ . Figure 6 shows the thermal expansion of both the  $Pbca$  and  $Pbca_E$  phases with respect to the equilibrium volume  $V_0$  at  $300 \text{ K}$ , together with the experimental values from refs 22 and 23, indicating that the evolution of  $V/V_0$  in  $Pbca$  at high temperatures is closer to the experimental value than in  $Pbca_E$ .



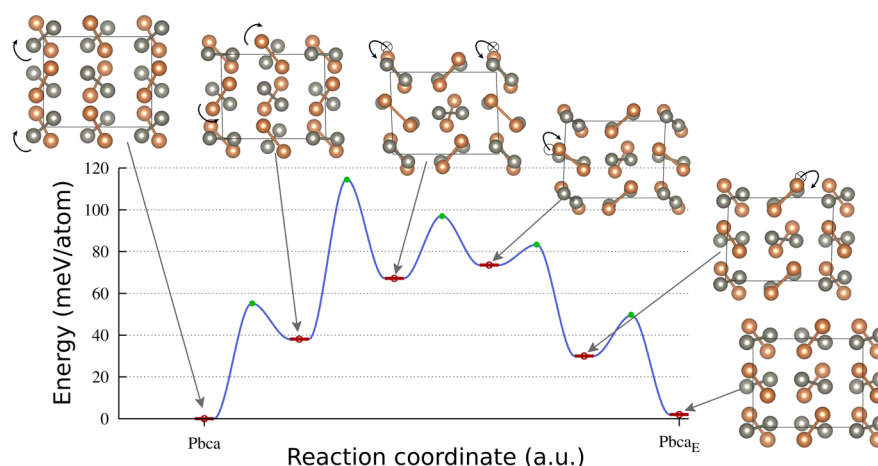


**Figure 4.** Energy along the transition pathway from the *Pbca* to the *Pbca<sub>E</sub>* phase, with local minima and saddle points denoted by red and green dots, respectively. The arrows indicate the dimer rotation involved in the structural transformation.

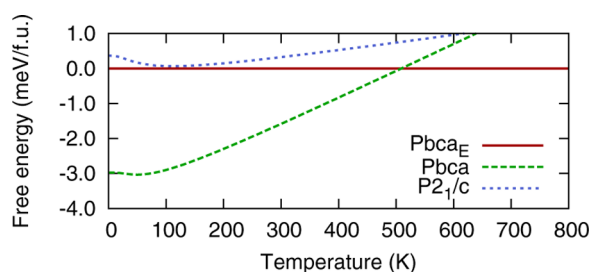


**Figure 5.** Free energy as a function of temperature.

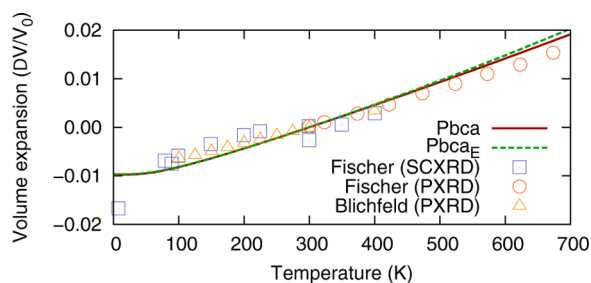


**Figure 6.** Comparison of the experimental and computed thermal expansion with respect to the volume  $V_0$  at a temperature of 300 K. The experimental values from SCXRD and PXRD measurements were taken from Fischer et al.<sup>22</sup> and Blichfeld and Iversen,<sup>23</sup> respectively, and the  $V_0$  were obtained from corresponding linear fits to the data points.

The atomic mean-square displacement tensors  $U_{ij}$  were computed as a function of temperature for both *Pbca* and *Pbca<sub>E</sub>* in order to investigate the harmonic thermal atomic displacements parameters (ADP)  $U_{eq}$  which is given by the average of the diagonal elements  $U_{eq} = \frac{\sum_i U_{ii}}{3}$ . Qualitatively, both *Pbca* and *Pbca<sub>E</sub>* exhibit a very similar behavior and agree well with experiments (see Figure S3). The differences between the two phases are only revealed when investigating the individual components  $U_{ii}$  of the ADP, which are shown in Figure 7 for *Pbca* and *Pbca<sub>E</sub>*, together with the experimental results from Fischer et al.<sup>22</sup> For the Zn atom in both *Pbca* and *Pbca<sub>E</sub>*, the  $U_{ii}$ 's have very similar values with  $U_{11} \approx U_{22} < U_{33}$ , which is in good agreement with the experiments from Fischer et al.<sup>22</sup> The Sb atoms, however, show a different behavior, where  $U_{11} < U_{22} < U_{33}$  for *Pbca<sub>E</sub>* but  $U_{22} < U_{11} < U_{33}$  for *Pbca*. Experimentally,

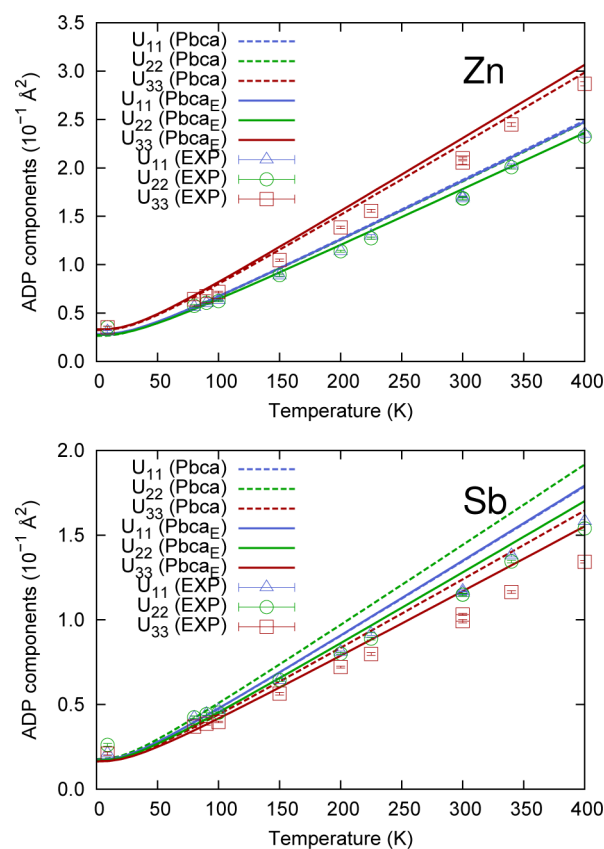


**Figure 7.** Components of the ADP for the Zn and Sb atoms in the *Pbca* and *Pbca<sub>E</sub>* phases, respectively. The experimental values were taken from Fischer et al.,<sup>22</sup> and the error bars indicate the  $\pm 2\sigma$  range. Note that, due to the difference in the labeling of the cell vector,  $U_{11}$  and  $U_{33}$  are exchanged compared to ref 22.

the measured ADP components behave like  $U_{11} < U_{22} < U_{33}$  in the temperature region above 100 K, which is in accordance with our DFT results of *Pbca<sub>E</sub>*. At  $T < 100$  K, however, the ordering of the ADP components changes, such that  $U_{11} \approx U_{33} < U_{22}$ , which is qualitatively closer to the calculated ADP of the *Pbca* phase. Thus, the observed inversion of the ADP components might be an evidence for *Pbca* in the ZnSb sample of Fischer et al.<sup>22</sup> at very low temperatures. However, this observation should be treated with caution, since the

relative error increases at low temperatures (see Figure 8d in ref 22).

Through a linear fit to the ADP, the Debye temperature  $\Theta_D$  can be estimated by

$$U_{eq} = \frac{3\hbar T}{mk_b \Theta_D} \quad (1)$$

for  $T > \Theta_D$ .<sup>38</sup> Our results for the  $Pbca_E$  phase are in excellent agreement with the DFT results of ref 22 (see Table 2). As

**Table 2. Debye Temperatures from a Linear Fit to the ADPs<sup>a</sup>**

atom	Fischer		Blichfeld	this work	
	EXP	DFT	EXP	$Pbca_E$	$Pbca$
$\Theta_D^{Zn}$ (K)	189	183	189	186	186
$\Theta_D^{Sb}$ (K)	186	169	180	170	165

<sup>a</sup>The reference values of Sb from Fischer et al.<sup>22</sup> were revised by using the correct atomic masses and refitting to the data points. The experimental values from Blichfeld and Iversen<sup>23</sup> are given in column 4.

pointed out by Blichfeld and Iversen,<sup>23</sup> the original values in ref 22 were computed with the wrong masses for Sb. The Debye temperature of Zn in the  $Pbca$  phase is almost identical to  $Pbca_E$ . The slightly lower value of  $\Theta_D^{Sb}$  in  $Pbca$  reflects the difference in the ADP components of the Sb as discussed above and could be responsible for a lower lattice thermal conductivity.

On the basis of the structural similarity between the low energy phases of ZnSb, we investigated the transformation kinetics between  $Pbca$  and  $Pbca_E$  by means of solid state nudged elastic band (SSNEB) calculations.<sup>39</sup> Since dimer rotations are associated with low energy phonon eigenmodes, the  $Pbca$  and  $Pbca_E$  structures were transformed into cells where the centers of the  $Sb_2^{4-}$  dimers were closely aligned with each other. Then, atomic indices of the structures were carefully matched to generate initial guesses for the SSNEB calculations which avoid dissociation of the  $Sb_2^{4-}$  dimers, resulting in three different pathways. After performing preliminary SSNEB simulations with loose convergence criteria, local minima along the pathways were identified and separate SSNEB calculations of higher accuracy were performed between each pair of the metastable structures. The pathway with the lowest barrier energy of 115 meV/atom (113 meV/atom for the reverse reaction) is shown in Figure 4, where each local minimum (red dots) along the path is illustrated separately such that the complete reaction can be divided into separate steps involving rotations of the  $Sb_2^{4-}$  dimers (arrows indicate the direction of rotation). The large number of low energy local minima connected through low barriers along the path is additional evidence of the glass-like energy landscape of the ZnSb system. In fact, the barrier heights are merely upper limits of the real transition energies, since only a concerted pathway in the smallest possible cell was studied without taking into account any nucleation effects. Such a barrier could thus be easily overcome at ambient conditions, allowing the transformation between the  $Pbca_E$  and the thermodynamically more stable  $Pbca$  phase.

The subtle structural difference in the  $Pbca$  and  $Pbca_E$  leads however to significant differences in both the electronic and transport properties. The electronic band structure of the  $Pbca$  phase is shown in Figure 8. Compared to the band structure of

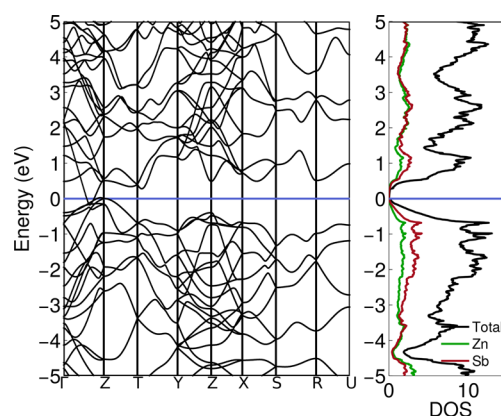


**Figure 8.** PBE electronic structure of the  $Pbca$  phase. Note the band-crossing at the Fermi level between  $\Gamma$  and Z which disappears in the HSE06 band structure.

$Pbca_E$  (see the Supporting Information), the conduction bands are shifted upward in energy in the  $\Gamma$ -X and  $\Gamma$ -Y directions, whereas in the  $\Gamma$ -Z direction they are shifted down, closing the small band gap (0.05 eV) observed in  $Pbca_E$ . Since it is well-known that conventional DFT band gaps are significantly underestimated,<sup>40</sup> we performed band structure calculations of higher accuracy using the Heyd-Scuseria-Ernzerhof hybrid functional (HSE06).<sup>41–43</sup> For the  $Pbca_E$  phase, the HSE06 gap is 0.58 eV and thus in excellent agreement with the experimental value of 0.61 eV at 4.2 K (0.50 eV at 300 K).<sup>44</sup> For the  $Pbca$  phase, the HSE06 functional opens a gap of 0.38 eV, a value well suited for TE applications.

The thermal conductivity  $\kappa$ , which affects the figure of merit  $ZT = \sigma S^2 T / \kappa$ , can be separated into the electronic ( $\kappa_e$ ) and lattice component ( $\kappa_L$ ), which allows us to rewrite  $ZT$  in a form which factorizes into a pure electronic part,  $S^2/L$ , modulated by the electronic fraction of the total thermal conductivity,

$$ZT = \frac{S^2}{L} \frac{\kappa_e}{\kappa_e + \kappa_L} < \frac{S^2}{L}$$

where  $L = \kappa_e / T\sigma$  is the Lorenz factor and  $S$  and  $L$  can be expressed as the ratio of the Onsager coefficients.<sup>45</sup> Therefore, the relaxation time  $\tau(\vec{k})$  for electrons cancels between the numerators and denominators if it is assumed to be wave vector independent. This allows us to obtain  $S^2/L$  without computing the details of the scattering of electrons, such that we can estimate an upper bound for the figure of merit. In this approximation,  $S^2/L$  is therefore a direct measure for the intrinsic quality of the electronic structure to convert heat into electricity.

The values of  $S^2/L$  are plotted in Figure 9 for  $Pbca_E$  and  $Pbca$  as a function of the carrier concentration. Across the whole range of carrier concentration, the values for  $Pbca$  and  $Pbca_E$  differ significantly. In the concentration range of interest for practical applications around 0.1 e per unit cell, the value of  $S^2/L$  is roughly 2.5 times higher for the  $Pbca$  than for the  $Pbca_E$  phase and up to 5 times higher if the doping is increased to an electron concentration of 0.3 e per unit cell. Therefore, the  $Pbca$  phase exhibits superior electronic transport properties in a promising range of carrier concentration.

In contrast to the electronic counterpart, the computation of the phonon scattering can not be avoided to obtain the lattice thermal conductivity. Within the relaxation time approximation,

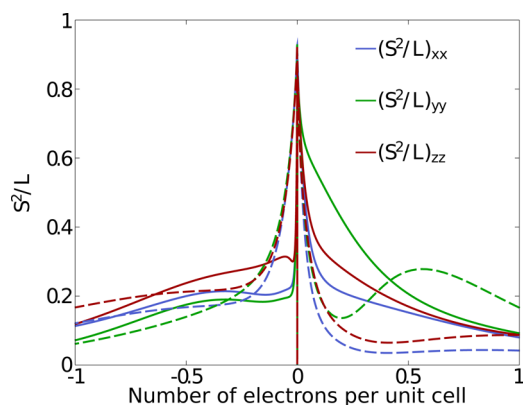


**Figure 9.** Reduced figure of merit  $S^2/L$  at  $T = 500$  K. Values for the  $Pbca$  structure are shown using solid lines while dashed lines are used for the  $Pbca_E$  structure.

the phonon Boltzmann equation can be solved in closed form to obtain the lattice thermal conductivity tensor,

$$\kappa_L = \frac{1}{V} \sum_{\mathbf{q}p} C_{\mathbf{q}p} \tau_{\mathbf{q}p} \mathbf{v}_{\mathbf{q}p} \otimes \mathbf{v}_{\mathbf{q}p} \quad (2)$$

where  $V$  is the unit cell volume and  $\mathbf{q}$  and  $p$ , respectively, are the wave vectors and branch index of the phonon states of frequency  $\omega_{\mathbf{q}p}$ , respectively.  $\mathbf{v}_{\mathbf{q}p} = \frac{\partial \omega_{\mathbf{q}p}}{\partial \mathbf{q}}$  is the phonon group velocity, and  $C_{\mathbf{q}p}$  is the mode dependent heat capacity given by

$$C_{\mathbf{q}p} = k_B \left( \frac{\hbar \omega_{\mathbf{q}p}}{k_B T} \right)^2 \frac{\exp\left(\frac{\hbar \omega_{\mathbf{q}p}}{k_B T}\right)}{\left[ \exp\left(\frac{\hbar \omega_{\mathbf{q}p}}{k_B T}\right) - 1 \right]^2}$$

and  $\tau_{\mathbf{q}p}$  is the phonon lifetime from phonon–phonon interactions:

$$\frac{1}{\tau_{\mathbf{q}p}} = \frac{36\pi}{\hbar^2} \sum_{\mathbf{q}'p'\mathbf{q}''p''} \left| \Phi_{-\mathbf{q}'\mathbf{q}''}^{pp'p''} \right|^2 \{ (n_{\mathbf{q}'p'} + n_{\mathbf{q}''p''} + 1) \delta(\omega_{\mathbf{q}p} - \omega_{\mathbf{q}'p'} - \omega_{\mathbf{q}''p''}) + (n_{\mathbf{q}'p'} - n_{\mathbf{q}''p''}) \delta(\omega_{\mathbf{q}p} + \omega_{\mathbf{q}'p'} - \omega_{\mathbf{q}''p''}) - (n_{\mathbf{q}'p'} - n_{\mathbf{q}''p''}) \delta(\omega_{\mathbf{q}p} - \omega_{\mathbf{q}'p'} + \omega_{\mathbf{q}''p''}) \}$$

where  $n_{\mathbf{q}p}$  is the Bose-Einstein occupation function of mode  $\mathbf{q}p$ . The  $\Phi_{-\mathbf{q}'\mathbf{q}''}^{pp'p''}$  describe the strength of the interaction between the three phonons ( $\mathbf{q}p$ ), ( $\mathbf{q}'p'$ ), and ( $\mathbf{q}''p''$ ) involved in the collisions. They correspond to the Fourier transform of the third order derivatives of the potential energy with respect to atomic displacements,  $\phi = \frac{\partial^3 E}{\partial u_i \partial u_j \partial u_k}$ , projected onto the phonon eigenvectors. The third order derivatives therefore represent the anharmonic contributions to the potential energy that generate the thermal resistivity within the lattice. This explicit calculation of the lattice thermal conductivity with the phono3py code<sup>46</sup> is the computationally most demanding task.

The lattice thermal conductivity is plotted as a function of temperature in Figure 10 together with measurements for the experimental  $Pbca_E$  phase,<sup>47–50</sup> indicating that values for  $Pbca$  are overall significantly lower than most experimental reports on  $Pbca_E$ . Compared to earlier theoretical results on  $Pbca_E$ , the

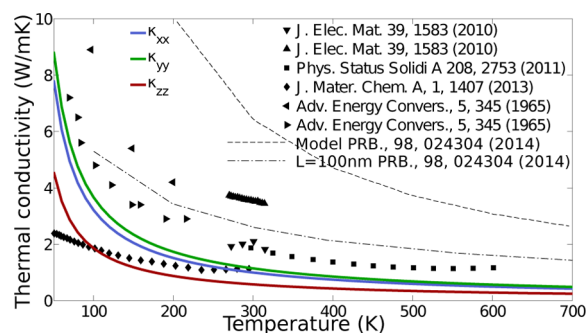


**Figure 10.** Lattice thermal conductivity as a function of temperature. The computed thermal conductivity for the  $Pbca$  phase is shown using solid lines. Experimental values for the  $Pbca_E$  phase are shown using the following symbols: ( $\blacktriangle$ ) no-ball-milled, ( $\blacktriangledown$ ,  $\blacksquare$ ) ball-milled, ( $\blacktriangleleft$ ) monocrystal, ( $\blacktriangleright$ ) polycrystal, and ( $\blacklozenge$ ) Zn point defects). The computational results of Bjerg et al.<sup>13</sup> are shown with dashed lines.

thermal conductivity of  $Pbca$  is by more than a factor 3 lower at 300 K (6.6 W/mK in ref 13). Experimentally, the lowest thermal conductivities were measured in microstructured and ball-milled samples ( $\blacktriangledown$  and  $\blacksquare$ ) and cold pressed samples containing Zn point defects ( $\blacklozenge$ ). It is well-known that defects, dislocations, interfaces, and grain boundaries strongly increase the phonon scattering and therefore decrease the thermal conductivity. These additional scattering processes are not included in our computations; nevertheless, our results produce thermal conductivities lower than those obtained from structurally engineered samples. In fact, the thermal conductivity of the  $Pbca$  phase is even lower than PbTe, the reference material for high performance TE ( $\sim 1.5$  W/mK at 500 K).<sup>51</sup> Furthermore, the value of 0.34 W/mK at 500 K along the  $z$ -axis in  $Pbca$  (corresponding to the direction along the rhomboidal chains) is even lower than the exceptionally low value ( $\sim 0.5$ – $1$  W/mK) reported for the  $Zn_4Sb_3$  alloy which, on the basis of this property, is considered one of the most promising TE materials.<sup>5</sup>

## CONCLUSION

In summary, a systematic search for low energy structures of the ZnSb compound was performed with first-principles electronic structure calculations, revealing the glass-like energy landscape and polymorphism of the ZnSb system. Two novel structures are predicted with competing energies to the known  $Pbca_E$  phase. The calculations show that the electronic transport properties of the putative ground state, the  $Pbca$  phase, are vastly superior to the  $Pbca_E$  structure. Simultaneously,  $Pbca$  also exhibits an exceptionally low thermal conductivity, which was for the very first time explicitly computed for a predicted material from *ab initio* calculations based on the third order derivatives of the potential energy. Therefore, this novel ZnSb polymorph exhibits all attributes to surpass known phases with respect to their efficiencies as TE materials. However, the free energy calculations predict that the  $Pbca$  is thermodynamically less stable than  $Pbca_E$  at operating temperatures of thermoelectric generators. Due to the low energy barriers associated with the rotation of  $Sb_2^{4-}$  dimers and its slightly larger volume, the  $Pbca$  phase might be synthesized through strain engineering or chemical pressure and is expected to be the ground state at low temperatures. A comparison of the ADP with the experimental results of Fischer et al.<sup>22</sup> indicates that the sample might have contained small fractions of the novel  $Pbca$  phase.



## ■ COMPUTATIONAL DETAILS

The structural search was performed with the minima hopping method,<sup>28,29</sup> which implements a highly reliable algorithm to identify the ground state structure of any material by efficiently sampling low lying phases on the energy landscape, based solely on the information on the chemical composition.<sup>52–54</sup> Consecutive short molecular dynamics escape steps are performed to overcome energy barriers followed by local geometry optimizations, while exploiting the Bell-Evans-Polanyi principle in order to accelerate the search.<sup>55,56</sup> The structural searches were conducted with cell sizes of 2, 4, and 8 formula units at discrete pressures of 0, 5, 10, and 20 GPa, scanning several hundred different structures. Initial structures were randomly generated.

The energies, forces, and stresses were evaluated with density functional theory calculations within the projector augmented wave (PAW) formalism<sup>57</sup> as implemented in the VASP<sup>58–60</sup> code together with the Perdew–Burke–Ernzerhof (PBE) approximation<sup>61</sup> to the exchange correlation potential. A plane-wave cutoff energy of 500 eV was used in conjunction with a sufficiently dense k-point mesh to ensure a convergence of the total energy to better than 1 meV/atom. Geometries were fully relaxed with a tight convergence criterion of less than 4 meV/Å for the maximal force components.

Transition pathways were computed using the VASP Transition State Theory Tools.<sup>39</sup> Initial pathways were roughly estimated through a solid state nudged elastic band (NEB) simulation. Saddle points were then refined by employing the climbing image NEB approach until the gradients were converged to less than 10 meV/Å.

High accuracy electronic band structure calculations were performed with the Heyd-Scuseria-Ernzerhof hybrid functional (HSE06)<sup>41–43</sup> as implemented in VASP. The electronic transport properties were computed using the BoltzTraP code.<sup>62</sup> Due to the semimetallic behavior of *Pbca* within PBE, we employed the modified Becke-Johnson meta-GGA functional<sup>63,64</sup> for all BoltzTraP calculations which was shown to give band gaps close to hybrid functionals at moderate computational cost (0.49 eV for *Pbca<sub>E</sub>*, 0.33 eV for *Pbca*). The slight underestimation of the gap is expected to introduce merely a simple shift in the temperature for the values of  $S^2/L$  when HSE06 is employed. The first Brillouin zone was sampled on a dense  $41 \times 41 \times 41$  mesh to ensure that the band structure was sufficiently converged.

Phonon calculations were carried out with the frozen phonon method as implemented in the phonopy<sup>65</sup> package. The lattice thermal conductivity was computed with the phono3py code.<sup>46</sup> Finite differences were used by displacing pairs of atoms by 0.01 Å from their equilibrium positions to obtain the forces on the atoms. For each of those configurations, a density functional calculation was performed for a 128 atoms supercell, with a dense k-point mesh of  $4 \times 4 \times 4$  and a plane wave cutoff energy of 400 eV. The different quantities appearing in eq 2 were finally computed on a uniform  $11 \times 11 \times 11$  grid in the first Brillouin zone.

## ■ ASSOCIATED CONTENT

### Supporting Information

The Supporting Information is available free of charge on the ACS Publications website at DOI: 10.1021/acs.chemmater.5b03856.

Crystallographic data of all structures discussed in this manuscript, listed together with a figure illustrating the local environment of the Sb atoms in the *Pbca<sub>E</sub>* and *Pbca* phases. Plot of the electronic band structures of the *Pbca<sub>E</sub>* and *Pbca* phases, provided together with plots comparing their ADPs and the ADP anisotropy factors. Table listing the energy differences between the *Pbca<sub>E</sub>* and *Pbca* structures with various approximations to the exchange-correlation functional. (PDF)

## ■ AUTHOR INFORMATION

### Corresponding Authors

\*E-mail: stefan.goedecker@unibas.ch.

\*E-mail: laurent.chaput@univ-lorraine.fr.

### Notes

The authors declare no competing financial interest.

## ■ ACKNOWLEDGMENTS

We thank Vinay Hegde and Dr. S. Shahab Naghavi for valuable expert discussions. Computational resources from GENCI-IDRIS under Grant 2014-x2014097186, the Swiss National Supercomputing Center (CSCS) in Lugano (project s499), and the National Energy Research Scientific Computing Center, which is supported by the Office of Science of the U.S. Department of Energy under Contract No. DE-AC02-05CH11231, are acknowledged. M.A. gratefully acknowledges support from the Novartis Universität Basel Excellence Scholarship for Life Sciences and the Swiss National Science Foundation. C.W. acknowledges support by the U.S. Department of Energy, Office of Science, Basic Energy Sciences, under Grant DEFG02-07ER46433. G.J.S. and W.G.Z. acknowledge the financial support of Solid-State Solar-Thermal Energy Conversion Center (S3TEC), an Energy Frontier Research Center funded by the U.S. Department of Energy, Office of Science, Basic Energy Sciences under Award No. DE-SC0001299.

## ■ REFERENCES

- (1) Snyder, G. J.; Toberer, E. S. Complex Thermoelectric Materials. *Nat. Mater.* **2008**, *7*, 105–114.
- (2) Rowe, D. *Thermoelectrics Handbook: Macro to Nano*; CRC Press: Boca Raton, FL, 2005.
- (3) Zhao, L.-D.; Lo, S.-H.; Zhang, Y.; Sun, H.; Tan, G.; Uher, C.; Wolverton, C.; Dravid, V. P.; Kanatzidis, M. G. Ultralow Thermal Conductivity and High Thermoelectric Figure of Merit in SnSe Crystals. *Nature* **2014**, *508*, 373–377.
- (4) Wright, D. A. Thermoelectric properties of Bismuth Telluride and Its Alloys. *Nature* **1958**, *181*, 834–834.
- (5) Snyder, G. F.; Christensen, M.; Nishibori, E.; Caillat, T.; Iversen, B. B. Disordered Zinc in  $\text{Zn}_4\text{Sb}_3$  with Phonon-Glass and Electron-Crystal Thermoelectric Properties. *Nat. Mater.* **2004**, *3*, 458.
- (6) Wu, H. J.; Zhao, L.-D.; Zheng, F. S.; Wu, D.; Pei, Y. L.; Tong, X.; Kanatzidis, M. G.; He, J. Q. Broad Temperature Plateau for Thermoelectric Figure of Merit  $ZT > 2$  in Phase-Separated  $\text{PbTe}_{0.7}\text{S}_{0.3}$ . *Nat. Commun.* **2014**, *5*, 4515.
- (7) Uher, C. In *Semiconductors and Semimetals*; Tritt, T. M., Ed.; Recent Trends in Thermoelectric Materials Research I; Elsevier: New York, 2001; Vol. 69; pp 139–253.
- (8) Nolas, G. S.; Slack, G. A.; Schujman, S. B. In *Semiconductors and Semimetals*; Tritt, T. M., Ed.; Recent Trends in Thermoelectric Materials Research I; Elsevier: New York, 2001; Vol. 69; pp 255–300.
- (9) Nolas, G. S.; Poon, J.; Kanatzidis, M. Recent Developments in Bulk Thermoelectric Materials. *MRS Bull.* **2006**, *31*, 199–205.
- (10) Seebeck, T. J. Ueber Die Magnetische Polarisation Der Metalle Und Erze Durch Temperatur-Differenz. *Ann. Phys.* **1826**, *82*, 133–160.
- (11) Benson, D.; Sankey, O. F.; Häussermann, U. Electronic Structure and Chemical Bonding of the Electron-Poor II-V Semiconductors  $\text{ZnSb}$  and  $\text{ZnAs}$ . *Phys. Rev. B: Condens. Matter Mater. Phys.* **2011**, *84*, 125211.
- (12) Jund, P.; Viennois, R.; Tao, X.; Niedziolka, K.; Tédénac, J.-C. Physical Properties of Thermoelectric Zinc Antimonide Using First-Principles Calculations. *Phys. Rev. B: Condens. Matter Mater. Phys.* **2012**, *85*, 224105.
- (13) Bjerg, L.; Iversen, B. B.; Madsen, G. K. H. Modeling the Thermal Conductivities of the Zinc Antimonides  $\text{ZnSb}$  and  $\text{Zn}_4\text{Sb}_3$ . *Phys. Rev. B: Condens. Matter Mater. Phys.* **2014**, *89*, 024304.

- (14) Sun, Y.; Christensen, M.; Johnsen, S.; Nong, N.; Ma, Y.; Sillassen, M.; Zhang, E.; Palmqvist, A.; Böttiger, J.; Iversen, B. Low-Cost High-Performance Zinc Antimonide Thin Films for Thermoelectric Applications. *Adv. Mater.* **2012**, *24*, 1693–1696.
- (15) Ahn, J. H.; Oh, M. W.; Kim, B. S.; Park, S. D.; Min, B. K.; Lee, H. W.; Shim, Y. J. Thermoelectric Properties of  $\text{Zn}_4\text{Sb}_3$  Prepared by Hot Pressing. *Mater. Res. Bull.* **2011**, *46*, 1490–1495.
- (16) Birkel, C.; Mugnaioli, E.; Gorelik, T.; Kolb, U.; Panthöfer, M.; Tremel, W. Solution Synthesis of a New Thermoelectric  $\text{Zn}_{(1+x)}\text{Sb}$  Nanophase and Its Structure Determination Using Automated Electron Diffraction Tomography. *J. Am. Chem. Soc.* **2010**, *132*, 9881–9889.
- (17) Pomrehn, G.; Toberer, E.; Snyder, G.; Van De Walle, A. Predicted Electronic and Thermodynamic Properties of a Newly Discovered  $\text{Zn}_8\text{Sb}_7$  Phase. *J. Am. Chem. Soc.* **2011**, *133*, 11255–11261.
- (18) Wang, J.; Kovnir, K. Elusive  $\beta\text{-Zn}_8\text{Sb}_7$ : A New Zinc Antimonide Thermoelectric. *J. Am. Chem. Soc.* **2015**, *137*, 12474–12477.
- (19) Okamura, C.; Ueda, T.; Hasezaki, K. Preparation of Single-Phase ZnSb Thermoelectric Materials Using a Mechanical Grinding Process. *Mater. Trans.* **2010**, *51*, 860–862.
- (20) Valsø, K.; Böttger, P. H. M.; Scherer, W.; Benson, D. E.; Wu, Y.; Eklöf, D.; Häussermann, U. Thermal and vibrational properties of thermoelectric ZnSb: Exploring the origin of low thermal conductivity. *Phys. Rev. B: Condens. Matter Mater. Phys.* **2015**, *91*, 224309.
- (23) Blichfeld, A. B.; Iversen, B. B. Fast direct synthesis and compaction of phase pure thermoelectric ZnSb. *J. Mater. Chem. C* **2015**, *3*, 10543–10553.
- (24) Izard, V.; Record, M. C.; Tedenac, J. C.; Fries, S. G. Discussion on the Stability of the Antimony zinc Binary Phases. *CALPHAD: Comput. Coupling Phase Diagrams Thermochem.* **2001**, *25*, 567–581.
- (25) Almin, K. E.; Hofman-Bang, N.; Gjertsen, P. The Crystal Structure of CdSb and ZnSb. *Acta Chem. Scand.* **1948**, *2*, 400–407.
- (26) Degtyareva, V. F.; Bdkin, I. K.; Khasanov, S. S. Crystalline and Amorphous States in Zn-Sb and Cd-Sb Alloys at High Pressure. *Phys. Solid State* **1997**, *39*, 1341–1344.
- (27) Tonkov, E. Y. *Compounds and Alloys Under High Pressure. A Handbook*; CRC Press: Boca Raton, FL, 1998.
- (28) Goedecker, S. Minima Hopping: An Efficient Search Method for the Global Minimum of the Potential Energy Surface of Complex Molecular Systems. *J. Chem. Phys.* **2004**, *120*, 9911.
- (29) Amsler, M.; Goedecker, S. Crystal Structure Prediction Using the Minima Hopping Method. *J. Chem. Phys.* **2010**, *133*, 224104.
- (30) De, S.; Willand, A.; Amsler, M.; Pochet, P.; Genovese, L.; Goedecker, S. Energy Landscape of Fullerene Materials: A Comparison of Boron to Boron Nitride and Carbon. *Phys. Rev. Lett.* **2011**, *106*, 225502.
- (31) Bjerg, L.; Madsen, G. K. H.; Iversen, B. B. Enhanced Thermoelectric Properties in Zinc Antimonides. *Chem. Mater.* **2011**, *23*, 3907–3914.
- (32) Hull, A. W.; Davey, W. P. Graphical Determination of Hexagonal and Tetragonal Crystal Structures from X-Ray Data. *Phys. Rev.* **1921**, *17*, 549–570.
- (33) Schiferl, D.; Cromer, D. T.; Jamieson, J. C. Structure Determinations on Sb up to  $85 \times 102$  MPa. *Acta Crystallogr., Sect. B: Struct. Crystallogr. Cryst. Chem.* **1981**, *37*, 807–810.
- (34) Kabalkina, S. S.; Mylov, V. P. Phase Transitions in Antimony at High Pressures. *Sov. Phys. Dokl.* **1964**, *8*, 917.
- (35) Aoki, K.; Fujiwara, S.; Kusakabe, M. New Phase Transition into the b.c.c. Structure in Antimony at High Pressure. *Solid State Commun.* **1983**, *45*, 161–163.
- (36) Schweika, W.; Hermann, R. P.; Prager, M.; Perßon, J.; Keppens, V. Dumbbell Rattling in Thermoelectric Zinc Antimony. *Phys. Rev. Lett.* **2007**, *99*, 125501.
- (37) Jund, P.; Viennois, R.; Tao, X.; Niedziolka, K.; Tedenac, J.-C. Physical Properties of Thermoelectric Zinc Antimonide Using First-Principles Calculations. *Phys. Rev. B: Condens. Matter Mater. Phys.* **2012**, *85*, 224105.
- (38) Willis, B. T. M.; Pryor, A. W. *Thermal Vibrations in Crystallography*; Cambridge University Press: New York, 1975.
- (39) Sheppard, D.; Xiao, P.; Chemelewski, W.; Johnson, D. D.; Henkelman, G. A Generalized Solid-State Nudged Elastic Band Method. *J. Chem. Phys.* **2012**, *136*, 074103–074103–8.
- (40) Perdew, J. P. Density Functional Theory and the Band Gap Problem. *Int. J. Quantum Chem.* **1985**, *28*, 497–523.
- (41) Heyd, J.; Scuseria, G. E.; Ernzerhof, M. Erratum: Hybrid Functionals Based on a Screened Coulomb Potential” [J. Chem. Phys. **118**, 8207 (2003)]. *J. Chem. Phys.* **2006**, *124*, 219906–219906–1.
- (42) Paier, J.; Marsman, M.; Hummer, K.; Kresse, G.; Gerber, I. C.; Ángyán, J. G. Erratum: Screened Hybrid Density Functionals Applied to Solids” [J. Chem. Phys. **124**, 154709 (2006)]. *J. Chem. Phys.* **2006**, *125*, 249901–249901–2.
- (43) Heyd, J.; Scuseria, G. E.; Ernzerhof, M. Hybrid Functionals Based on a Screened Coulomb Potential. *J. Chem. Phys.* **2003**, *118*, 8207–8215.
- (44) Komiya, H.; Masumoto, K.; Fan, H. Y. Optical and Electrical Properties and Energy Band Structure of ZnSb. *Phys. Rev.* **1964**, *133*, A1679–A1684.
- (45) Mahan, G. D. *Solid State Phys.* **1997**, *51*, 81–157.
- (46) Togo, A.; Chaput, L.; Tanaka, I. Distributions of Phonon Lifetimes in Brillouin Zones. *Phys. Rev. B: Condens. Matter Mater. Phys.* **2015**, *91*, 094306.
- (47) Fay, B.; Justi, E.; Schneider, G. Wärmeleitfähigkeit Und Thermokraft Von ZnSb Bei Tiefen Temperaturen. *Adv. Energy Convers.* **1965**, *5*, 345.
- (48) Eklöf, D.; Fischer, A.; Wu, Y.; Scheidt, E.-W.; Scherer, W.; Häussermann, U. Transport Properties of the II-V Semiconductor ZnSb. *J. Mater. Chem. A* **2013**, *1*, 1407.
- (49) Böttger, P. H. M.; Pomrehn, G. S.; Snyder, G. J.; Finstad, T. G. Doping of P-Type ZnSb: Single Parabolic Band Model and Impurity Band Conduction. *Phys. Status Solidi A* **2011**, *208*, 2753.
- (50) Böttger, P. H.; Valsø, K.; Deledda, S.; Finstad, T. G. Influence of Ball-Milling, Nanostructuring, and Ag Inclusions on Thermoelectric Properties of ZnSb. *J. Electron. Mater.* **2010**, *39*, 1583.
- (51) Heremans, J. P.; Jovovic, V.; Toberer, E. S.; Saramat, A.; Kurosaki, K.; Charoenphakdee, A.; Yamanaka, S.; Snyder, G. J. Enhancement of Thermoelectric Efficiency in PbTe by Distortion of the Electronic Density of States. *Science* **2008**, *321*, 554–557.
- (52) Amsler, M.; Flores-Livas, J. A.; Lehtovaara, L.; Balima, F.; Ghasemi, S. A.; Machon, D.; Pailhès, S.; Willand, A.; Caliste, D.; Botti, S.; San Miguel, A.; Goedecker, S.; Marques, M. A. L. Crystal Structure of Cold Compressed Graphite. *Phys. Rev. Lett.* **2012**, *108*, 065501.
- (53) Flores-Livas, J. A.; Amsler, M.; Lenosky, T. J.; Lehtovaara, L.; Botti, S.; Marques, M. A. L.; Goedecker, S. High-Pressure Structures of Disilane and Their Superconducting Properties. *Phys. Rev. Lett.* **2012**, *108*, 117004.
- (54) Amsler, M.; Flores-Livas, J. A.; Huan, T. D.; Botti, S.; Marques, M. A. L.; Goedecker, S. Novel Structural Motifs in Low Energy Phases of  $\text{LiAlH}_4$ . *Phys. Rev. Lett.* **2012**, *108*, 205505.
- (55) Roy, S.; Goedecker, S.; Hellmann, V. Bell-Evans-Polanyi Principle for Molecular Dynamics Trajectories and Its Implications for Global Optimization. *Phys. Rev. E* **2008**, *77*, 056707.
- (56) Sicher, M.; Mohr, S.; Goedecker, S. Efficient Moves for Global Geometry Optimization Methods and Their Application to Binary Systems. *J. Chem. Phys.* **2011**, *134*, 044106.
- (57) Blöchl, P. E. Projector Augmented-Wave Method. *Phys. Rev. B: Condens. Matter Mater. Phys.* **1994**, *50*, 17953–17979.
- (58) Kresse, G. Ab-Initio Molecular-Dynamics for Liquid-Metals. *J. Non-Cryst. Solids* **1995**, *192–193*, 222–229.
- (59) Kresse, G.; Furthmüller, J. Efficiency of Ab-Initio Total Energy Calculations for Metals and Semiconductors Using a Plane-Wave Basis Set. *Comput. Mater. Sci.* **1996**, *6*, 15–50.



- (60) Kresse, G.; Joubert, D. From Ultrasoft Pseudopotentials to the Projector Augmented-Wave Method. *Phys. Rev. B: Condens. Matter Mater. Phys.* **1999**, *59*, 1758–1775.
- (61) Perdew, J. P.; Burke, K.; Ernzerhof, M. Generalized Gradient Approximation Made Simple. *Phys. Rev. Lett.* **1996**, *77*, 3865–3868.
- (62) Madsen, G. K. H.; Singh, D. J. BoltzTraP. a Code for Calculating Band-Structure Dependent Quantities. *Comput. Phys. Commun.* **2006**, *175*, 67.
- (63) Becke, A. D.; Johnson, E. R. A Simple Effective Potential for Exchange. *J. Chem. Phys.* **2006**, *124*, 221101.
- (64) Tran, F.; Blaha, P. Accurate Band Gaps of Semiconductors and Insulators with a Semilocal Exchange-Correlation Potential. *Phys. Rev. Lett.* **2009**, *102*, 226401.
- (65) Togo, A.; Oba, F.; Tanaka, I. First-Principles Calculations of the Ferroelastic Transition Between Rutile-Type and CaCl<sub>2</sub>-Type SiO<sub>2</sub> at High Pressures. *Phys. Rev. B: Condens. Matter Mater. Phys.* **2008**, *78*, 134106.